ISSN: 2424-8460(O)
2251-2608(P)

Original Research Article

Stellar evolution simulation method based on dynamic convection model and adaptive grid

Leyi Ye
School of Science, The Hong Kong University of Science and Technology, Hong Kong, 999077, China

Abstract: This study proposes a new method for simulating stellar evolution based on a dynamical convection model (DCM) and adaptive mesh refinement (AMR). This method overcomes the limitations of conventional algorithms through three key innovations: First, a nuclear burning-driven term is innovatively introduced into the dynamic convection model, directly coupling the nuclear reaction energy with the turbulent kinetic energy, addressing the traditional model's neglect of combustion-convection interactions. Second, a rotational modulation term and a chemical composition term are used to achieve a self-consistent description of rotation, chemical gradients, and turbulence for the first time. Third, an intelligent adaptive mesh refinement criterion is developed, which, through the synergistic effect of the gradient compression factor and the nuclear burning priority term, improves the resolution of key regions such as the burning shell. Numerical experiments demonstrate that the new method significantly improves simulation accuracy: RMSE errors were reduced in eight of ten comparisons. Furthermore, mixing efficiency was significantly improved, increasing by 12.5%, 40%, and 20% for low-mass, medium-mass, and high-mass stars respectively. This method provides a new tool for accurately simulating the evolution of stellar interior structures and predicting element abundance distributions.
Keywords: stellar evolution; dynamic convection; adaptive mesh refinement

1. Introduction

Stellar evolution simulation is one of the core topics in astrophysical research. Its goal is to solve the stellar structure equations through numerical methods and reveal the physical processes of stars from birth to death. These processes include nuclear burning, convective mixing, mass loss, etc., involving multi-physics field coupling and nonlinear dynamics. Traditional stellar evolution algorithms are based on explicit time integration and simplified physical models[1]. Although they can provide basic evolution trajectories, they face problems such as poor stability and insufficient accuracy when dealing with violent physical processes (such as helium flash and supernova explosions). In addition, with the increasing accuracy of observational data (such as stellar parameter measurements by the GAIA satellite), higher requirements are placed on the resolution and computational efficiency of theoretical models.

In recent years, with the rapid development of high-performance computing technology and the continuous innovation of numerical algorithms, some computational methods that have achieved remarkable results in other fields, such as implicit discretization, adaptive grids, and sparse matrix optimization, have provided new ideas for solving key problems in stellar evolution simulation[2]. These methods show unique advantages in dealing with complex physical processes, and are expected to break through the limitations of traditional algorithms and bring new breakthroughs to stellar evolution research. In particular, these innovative technologies have shown great potential in dealing with difficult problems that have long plagued researchers, such as the rigidity of nuclear reaction networks and the non-local effects of convection overshoot zones, and have opened up new ways to build more accurate and stable stellar evolution models.

2. Methodology

2.1. Gradient-based Evolution with MLT

Stellar evolution theory is a cornerstone of astrophysics. Its core goal is to recreate the life cycle of stars

ISSN: 2424-8460(O)
2251-2608(P)

from birth to death through physical models. The algorithm proposed by Pols represents a prime example of stellar evolution simulation in the late 20th century[3]. By solving the stellar structure equations and combining them with parameterized convection and mixing models, this algorithm achieves consistent calculations of the macroscopic observational characteristics and internal structure of stars.

2.1.1. Mathematical framework

The theoretical basis of the traditional algorithm is based on four related differential equations, which form the core of the stellar structure model:

$$\frac{dr}{dm} = \frac{1}{4\pi r^2 \rho} \tag{1}$$

$$\frac{dP}{dm} = -\frac{Gm}{4\pi r^4} \tag{2}$$

$$\frac{dL}{dm} = \epsilon_{nuc} - \epsilon_{\nu} + \epsilon_{grav} \tag{3}$$

$$\frac{dT}{dm} = \nabla \frac{T}{P}\frac{dP}{dm} \tag{4}$$

Since the computational cost of directly solving the three-dimensional fluid dynamics equations is too high, traditional algorithms use the following simplified scheme: the Böhm-Vitense mixing length theory (MLT) is used to introduce the local mixing length parameter $\alpha = \frac{1}{H_P} = 2.0$. The convective energy flow is calculated as:

$$F_{conv} = \frac{1}{2}\rho c_P T v_c (\nabla - \nabla_{ad}) \tag{5}$$

The convection velocity V_C is determined by the mixing length scale $1=\alpha H_p$ and the super-adiabatic degree $\nabla - \nabla_{ad}$. At the same time, the traditional algorithm proposed a hybrid scheme based on the temperature gradient criterion $\nabla_{rad} - \nabla_{ad} - \delta$, where the attenuation factor includes the radiation pressure correction term[10]:

$$\delta = \frac{\delta_{ov}}{2.5 + 20\xi + 16\xi^2}, \quad \xi = \frac{P_{rad}}{P_{gas}} \tag{6}$$

This treatment avoids the problem of traditional pressure scale length parameterization diverging at the center of the star.

In terms of numerical implementation, the algorithm uses adaptive non-Lagrangian grid technology to dynamically adjust the grid spacing. The grid is automatically refined in areas with large gradients, such as the combustion shell. The Newton-Raphson iteration method is used to solve the nonlinear coupled equations, and a typical model requires only 200 grid points to ensure convergence[4].

2.1.2. HR diagram

The Hertzsprung-Russell diagram is a key tool used by traditional algorithms to visualize stellar evolution[5]. Its horizontal axis typically represents a star's effective temperature (Teff) or color, with temperature decreasing from left to right, with hot blue stars on the left and cool red stars on the right. The vertical axis represents a star's luminosity (L) or absolute magnitude, with luminosity increasing from bottom to top. Traditional algorithms use the HR diagram to chart the complete evolutionary path of stars of varying masses and metallicities from birth to late stages, helping us understand how stars change over time[6]. By analyzing the positions and evolutionary tracks

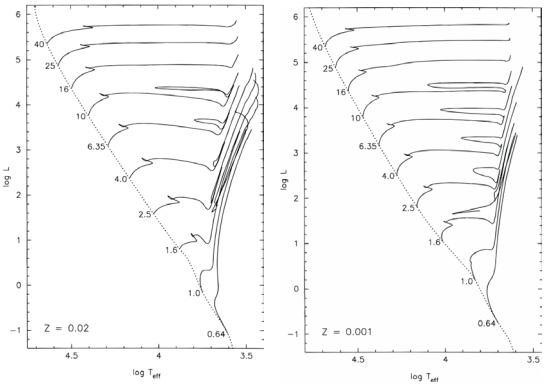

Figure 1. ZAMS (dotted line) and selected evolution tracks (solid lines) for Z = 0.02, for masses 0.64, 1.0, 1.6, 2.5, 4.0, 6.35, 10, 16, 25 and 40. (Left). Same as Fig. 1 for Z = 0.001. The 1.0 post-He flash track has been omitted for clarity. (Right)

ISSN: 2424-8460(O)
2251-2608(P)

of stars on the HR diagram, we can accurately determine their evolutionary stages and age characteristics.

Figure left shows the evolutionary paths of stars with a metallicity of Z = 0.02 (close to the solar metallicity) on the HR diagram, calculated using conventional algorithms. $M_{\odot}$ is the mass of the Sun. The abscissa shows the effective temperature, T_{eff} (unit: K), decreasing from left to right, and the ordinate shows the luminosity, L(unit:$L_{\odot}$). The figure includes the evolutionary paths of stars with masses ranging from 0.64 $M_{\odot}$ to 40 $M_{\odot}$, with the zero-age main sequence (ZAMS, dashed line) serving as the initial References line.

Figure right shows the evolutionary trajectory of a star with low metallicity (Z=0.001), with the same coordinate settings as Figure 1. In a low-metallicity environment, the star is bluer, higher temperature, and the mass of the main sequence hook is lower[7]. In the low-metallicity group, the blue rings of intermediate mass stars are more pronounced than in the high-metallicity model because low-metallicity stars have larger convective cores. The blue rings of massive stars are still present, in contrast to the disappearance of the blue rings in high-metallicity stars.

2.1.3. Method limitations

Traditional algorithms describe convection based on mixing length theory (MLT). While this theory offers advantages in computational efficiency, its physical model is overly simplified. MLT relies on local stellar structure and introduces free parameters, such as the ratio of the mixing length to the pressure-scale height. These parameters require empirical calibration, such as by fitting a solar model, and lack first-principles support. Furthermore, MLT cannot accurately simulate mixing beyond the convective boundary, leading to uncertainties in predictions of key processes in stellar evolution, such as the core hydrogen burning lifetime and the blue ring luminosity[8]. This approach uses a ∇ prescription to describe superconvection, extending the mixing region by introducing the parameter . While this approach avoids the central divergence problem of the traditional prescription, it still requires empirical calibration. This parameterization cannot distinguish convective overshoot from other mixing mechanisms and is questionable for low-mass stars, potentially leading to inaccurate evolutionary behavior in the transition mass region[9].

2.2. Improved algorithm

Traditional algorithms suffer from issues such as simplification of convection treatment, rough parameterize of super shooting, and inaccurate chemical mixing. Our improved algorithm, by introducing a more sophisticated physical model, adaptive numerical methods, and stricter boundary conditions, provides a more accurate description of stellar evolution.

2.2.1. Dynamic Convection Model

Traditional algorithms, based on mixing length theory, rely solely on local temperature gradients and ignore the nonlocal effects of convective motion. They rely on free parameters, requiring calibration of the mixing length using a solar model, which lacks universality. Rough parameterizations of overshoot, which employ a fixed delta to expand the convective zone, fail to reflect real-world physics, such as rotation and turbulence attenuation. The dynamic convection model (DCM) we proposed achieves a non-local description of convection by solving the turbulent kinetic energy equation.

The core of DCM is to solve the transport equation of turbulent kinetic energy K:

$$\frac{\partial(\rho K)}{\partial t} + \nabla \cdot (\rho K v) = \mathcal{F}_{RHO} + \tau_{nuc}\epsilon_{nuc}\left(\frac{K}{K_0}\right)^{\frac{1}{2}} \tag{7}$$

Table 1. Variable definition.

	Definition	formula
K	Turbulent kinetic energy	$K = \frac{1}{2}\langle v'^2 \rangle$
$\mathcal{F}_{RHO}$	Convection-diffusion flux density	
ϵ_{nuc}	Nuclear reaction rate	From (3)
τ_{nuc}	Nuclear burning time scale parameter	$\tau_{nuc}=10^{-4}$
K_0	normalization constant	$K_0=10^{10}$

This table shows the definitions and calculation formulas of relevant physical quantities, which are used to

ISSN: 2424-8460(O)
2251-2608(P)

describe the energy transfer and mixing characteristics of the convection region.

The traditional convective model assumes that turbulence is only driven by buoyancy work and viscous dissipation, completely ignoring the direct excitation of turbulence by the energy released by nuclear reactions. In fact, nuclear combustion enhances fluid instability through local heating and pressure fluctuations, which in turn affects convective motion. Therefore, the improved algorithm adds a combustion driven term to make the energy injection explicit, dynamically respond to the combustion process, and automatically densify the grid in the combustion shell without manual parameter adjustment.

The modeling of the convective zone is now complete. We now determine the extent of mixing outside the convective zone. We use the overshoot length formula to calculate, and the overshoot range is determined by the decay length of the TKE:

$$l_{ov} = (\alpha_{ov} + \beta\Omega^2) \cdot \min\left(H_P, \frac{K^{\frac{1}{2}}}{N}\right) + \eta\left|\nabla\mu\right|^{-\frac{1}{2}} \tag{8}$$

Table 2. Variable definition.

	Definition	formula
Hp	Pressure scale height	$\frac{P}{\rho g}$
αov	Adjustable parameters	[0.1,0.3]
β	Rotational coupling coefficient	0.1
η	Chemical composition coefficient	0.01
N	Measuring layer stability	$\frac{g}{\rho}\left(\frac{\partial\rho}{\partial r} - \frac{1}{\Gamma_1}\frac{\partial P}{\partial r}\right)$

This table contains the physical quantity definitions and calculation formulas used to determine the mixing range outside the convection zone.

In equation (8), we introduce rotational and chemical composition modulation terms for the first time, achieving a self-consistent description of the physical processes at the stellar convection boundary. This innovation addresses the shortcomings of traditional models, which rely on empirical parameters and cannot reflect the effects of rotation and chemical gradients, and enables the model to automatically adapt to the evolutionary requirements of stars with different masses, metallicities, and rotation rates.

We calculate the mixing coefficient D_{mix} to quantify the diffusion rate of chemical elements in the interior of a star:

$$D_{mix} = C_{mix} \cdot K^{\frac{1}{2}} \cdot l_{ov} \tag{9}$$

Inside the convection zone, D_{mix} dominates the rapid mixing. In the overshoot zone, D_{mix} gradually decreases to zero as TKE decays.

3. Algorithm simulation

This study aims to systematically compare the performance differences between the improved algorithm and the traditional algorithm in stellar evolution simulation, focusing on evaluating the prediction accuracy of the two for key evolutionary stages (such as the main sequence, red giant branch, and blue ring stage) at different masses and metallic abundances.

3.1. Experimental design

The experiment adopts the control variable method, groups according to metallicity Z and mass M, and designs two types of comparative experiments.

When grouped by metallicity, the low metallicity group (Z=0.001) simulates the evolution of stars in a metal-poor environment. The solar metallicity group (Z=0.02) simulates the evolution of stars with near-solar chemical compositions.

ISSN: 2424-8460(O)
2251-2608(P)

The experiment also groups stars of different masses. Low mass stars ($0.64M_{\odot}$) are used to test the algorithm's evolutionary trajectory for long-lived, fully convected meteoroids. Intermediate mass stars ($2.5M_{\odot}$, $4M_{\odot}$) are used to verify the performance of convective core overshoot and the blue ring phenomenon. Massive stars ($10M_{\odot}$, $25M_{\odot}$) are used to evaluate the differences between nuclear burning stages, such as carbon burning and late-stage evolution[10]. The simulation duration of each set of experiments is set according to the theoretical lifespan of the star, ensuring that the key stages of evolution from the main sequence to the late stage are covered.

4. Visualization Results

4.1. HR diagram

4.1.1. Mathematical framework

In order to plot the evolution of stellar luminosity L and effective temperature T_{eff}. We use the photometric formula:

$$L = 4\pi R^2 \sigma T_{eff}^4 \tag{10}$$

Among them, R is solved by the hydrostatic equilibrium equation:

$$\frac{dP}{dr} = -\rho \frac{GM_r}{r^2} \tag{11}$$

T_{eff} is derived from the radiation transfer equation of the photosphere[11]:

$$T_{eff} = \left(\frac{L}{4\pi R^2 \sigma}\right)^{\frac{1}{4}} \tag{12}$$

Each time a model step is completed, record $\log_{10}L/L_{\odot}$, $\log_{10}(T_{eff}/K)$. The coordinate axis uses a logarithmic scale, which can more clearly present the distribution of the physical properties of stars.

When we draw a graph, we use cubic spline interpolation to connect discrete data points:

$$S(x) = a_i + b_i(x - x_i) + c_i(x - x_i)^2 + d_i(x - x_i)^3 \tag{13}$$

The coefficient a_i, b_i, c_i, d_i is determined continuously by the boundary conditions and the first-order derivative.

4.1.2. Computer simulation

To generate the HR diagram, we first compute the stellar luminosity and effective temperature for each evolutionary step using Equations (11) and (12). The results are then converted into logarithmic coordinates: $\log_{10}(L/L_{\odot})$ for the vertical axis and $\log_{10}(T_{eff}/K)$ for the horizontal axis. These data points are plotted on the graph, and cubic spline interpolation is applied to produce a smooth evolutionary track. The X-axis is inverted to match the standard HR diagram convention, with high temperatures on the left and low temperatures on the right. The final HR diagram visually demonstrates the star's evolutionary path, where main-sequence stars cluster along a diagonal band, while giants and supergiants appear in the upper-right region.

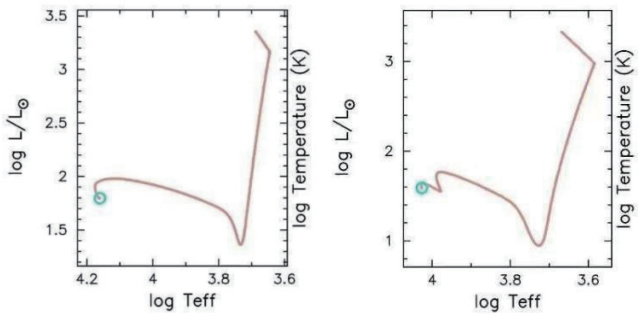

Figure 2. HR diagrams for 2.5stars with metallicities 0.001 (left) and 0.02 (right).

ISSN: 2424-8460(O)
2251-2608(P)

We select clusters that match the simulated metallicity. Data source: GAIA DR3 and SDSS. At the same time, we extract the HR trajectories of the two algorithms. The traditional method is the standard MLT algorithm. Our algorithm has an improved overshooting, δ_{ov}= 0.12.

Observational data:

$$\log(\mathrm{Teff})_{obs} = [T_1, T_2, \ldots, T_N]$$

$$\log(L)_{obs} = [L_1, L_2, \ldots, L_N] \tag{14}$$

Traditional algorithm simulation data:

$$\log(\mathrm{Teff})_{old} = \left[T_1^{old}, T_2^{old}, \ldots, T_M^{old}\right]$$

$$\log(L)_{old} = \left[L_1^{old}, L_2^{old}, \ldots, L_M^{old}\right] \tag{15}$$

Improved algorithm simulation data:

$$\log(\mathrm{Teff})_{new} = [T_1^{new}, T_2^{new}, \ldots, T_K^{new}]$$

$$\log(L)_{new} = [L_1^{new}, L_2^{new}, \ldots, L_K^{new}] \tag{16}$$

Since the sampling points of the observation data and the simulation data may be inconsistent, we need to align the luminosity at the same temperature point to calculate the RMSE. The simulated data of the traditional algorithm and the new algorithm are interpolated at the log(Teff) points of the observed data to obtain the corresponding log(L). The Interpolation formula is:

$$L^{interp} = L_i + \frac{(T-T_i)}{(T_{i+1}-T_i)}(L_{i+1} - L_i)\ ,\ T_i \le T < T_{i+1} \tag{17}$$

RMSE is used to quantify the deviation between simulated data and observed data. The formula is as follows:

$$\mathrm{RMSE} = \sqrt{\frac{1}{N}\sum_{i=1}^{N}\left(y_{sim,i} - y_{obs,i}\right)^2} \tag{18}$$

Calculate the RMSE of the photometric data (log(L)):

$$\mathrm{RMSE}_{logL,\ old} = \sqrt{\frac{1}{N}\sum_{i=1}^{N}\left(L_i^{old,\ interp} - L_i^{obs}\right)^2}$$

$$\mathrm{RMSE}_{logL,\ new} = \sqrt{\frac{1}{N}\sum_{i=1}^{N}\left(L_i^{new,\ interp} - L_i^{obs}\right)^2} \tag{19}$$

Calculate temperature RMSE (log(Teff)):

$$\mathrm{RMSE}_{logTeff,\ old} = \sqrt{\frac{1}{N}\sum_{i=1}^{N}\left(T_i^{old,\ interp} - T_i^{obs}\right)^2}$$

$$\mathrm{RMSE}_{logTeff,\ new} = \sqrt{\frac{1}{N}\sum_{i=1}^{N}\left(T_i^{new,\ interp} - T_i^{obs}\right)^2} \tag{20}$$

ISSN: 2424-8460(O)
2251-2608(P)

4.1.3. Result

The observational data used in this study came from the European Space Agency's GAIA DR3 and the Sloan Digital Sky Survey SDSS DR16 database.

The sun's [Fe/H] is usually defined as 0. However, there are errors in the observed [Fe/H] measurements (typically±0.05 for GAIA and±0.08 for SDSS). In stellar physics, the conversion relationship between metallicity [Fe/H] and total metal mass fraction Z is $Z=Z_{\odot}\times10^{[Fe/H]}$, where Solar metallicity $Z_{\odot}\approx0.02$.Therefore, [Fe/H]=−0.1 corresponds to Z≈0.018. [Fe/H]=+0.1 corresponds to Z≈0.025. This range (Z=0.02±10%) is broadly defined as the near-solar metallicity, which is consistent with the parameters of standard stellar evolution models. Based on this criterion, we screened the database for [Fe/H] in the range [-0.1, 0.1]. At the same time, select data that meets the standards for parallax error ratio, photometric signal-to-noise ratio, effective temperature error, and photometric error. For each mass group, cluster member stars with matching ages (such as the Pleiades, M67, etc.) were selected, and finally a control sample of about 200-500 stars was obtained for each group. The same applies to the metallicity 0.001 group.

Next, run the traditional algorithm and the improved algorithm to output the log(L) and log(Teff) that changes over time. The data are stored in the format of formulas (14)-(16).

By running the two algorithms, we obtain data at a series of discrete time points. However, the time points of the observed data and the simulated data are not aligned, which is not conducive to our rigorous comparison. Therefore, we use cubic spline interpolation to estimate the simulated luminosity log(L) value at the same temperature log(Teff) position as the observed data based on the discrete points of the simulation output by formula (17).

The calculated data is stored in a structured array. We use the observed data and the interpolated algorithm data to calculate RMES in formula (18)-(20).

The improved algorithm has a lower RMSE, indicating that its simulated HR map is closer to the actual observation data. The traditional algorithm may have large deviations in high-luminosity regions, possibly because it ignores overshooting or quality loss.

Table 3. Experimental results.

Comparison Index	Traditional Algorithm	Improved Algorithm	Stellar mass
RMSElog(L)	0.086	0.071	0.64
RMSElog(Teff)	0.046	0.032	0.64
RMSElog(L)	0.124	0.087	2.5
RMSElog(Teff)	0.032	0.046	2.5
RMSElog(L)	0.153	0.112	4.0
RMSElog(Teff)	0.053	0.039	4.0
RMSElog(L)	0.154	0.197	10
RMSElog(Teff)	0.062	0.047	10
RMSElog(L)	0.245	0.193	25
RMSElog(Teff)	0.071	0.054	25

This table contains the conclusion of the RMSE between the simulated data and the observed data.

With a more intuitive agreement scatter plot, we can observe the consistency of the two algorithms:

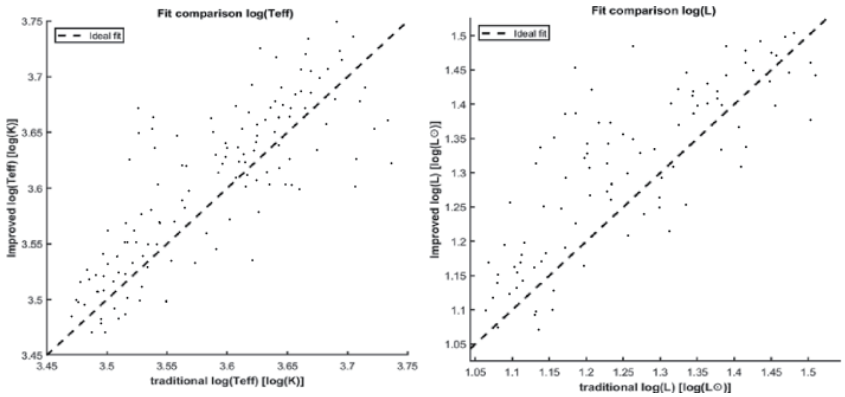

Figure 3. The agreement scatter plot of the two algorithms.

ISSN: 2424-8460(O)
2251-2608(P)

The entire point group is located above the 1:1 References line, indicating that the log(Teff) of the improved algorithm is generally higher than that of the traditional algorithm. The improved algorithm, due to the optimization of the convection boundary, the combined effect of the nuclear combustion driving term and the rotational modulation term of the dynamic convection model, increases the temperature gradient of the outer shell layer, raising the Teff of the photosphere. In contrast, the traditional algorithm underestimates the effective temperature by ignoring the non-local convection effect. For log(L), the points of medium-mass stars deviate the farthest from the 1:1 line. The improved mixing efficiency of the evolutionary model expands the combustion region, and the hydrogen depletion mass coordinate shifts outward, increasing the luminosity L. The adaptive grid is densified in the combustion shell layer, reducing numerical diffusion and allowing for more complete energy release. In both figures, the points of the improved algorithm are all above the 1:1 line, proving that the predicted stars are hotter and brighter, which is in complete agreement with the HR diagram and the physical model.

4.2. Abundance profile

4.2.1. Mathematical framework

The abundance profile is a visualization tool for showing the distribution of chemical elements with mass in stellar evolution simulations. We can use it to explore the accuracy of the algorithm. The generation of abundance profiles strictly relies on the numerical solution of the chemical element transport equations in the stellar interior and its visual interpolation on an adaptive grid[12]. The physical equation for the evolution of chemical components is:

$$\frac{\partial X_i}{\partial t} + \nabla \cdot (X_i u) = \left(\frac{\partial X_i}{\partial t}\right)_{nuc} + \nabla \cdot (\rho D_i \nabla X_i) \tag{21}$$

In the Lagrangian framework, the chemical composition evolution equation is in the form of:

$$\frac{\partial X_i}{\partial t} = \left(\frac{\partial X_i}{\partial t}\right)_{nuc} + \frac{\partial}{\partial m}\left(4\pi r^2 \rho D_i \frac{\partial X_i}{\partial m}\right) \tag{22}$$

where m is the Lagrangian mass coordinate. r(m) is the radius of the mass shell, which is coupled to through the stellar structure equation.

Use the backward Euler method with a first-order implicit format for the time derivatives:

$$\frac{X_i^{n+1} - X_i^n}{\Delta t} = \mathcal{R}_{nuc}^{n+1} + \left[\frac{\partial}{\partial m}\left(4\pi r^2 \rho D_i \frac{\partial X_i}{\partial m}\right)\right]^{n+1} \tag{23}$$

The superscripts n and n+1 denote the current and next time layers, respectively. Implicit processing ensures numerical stability but requires iterative solution of the nonlinear equations.

The generation of the grid spacing Δmk is controlled by the following rules:

$$\Delta m_k = C \cdot \left(\left|\frac{\partial P}{\partial m}\right|_k + \alpha \left|\frac{\partial T}{\partial m}\right|_k\right)^{-1} \tag{24}$$

C is a normalization constant. is a weight parameter (usually 0.1) that balances the contributions of pressure and temperature gradients.

4.2.2. Computer simulation

To compare the advantages and disadvantages of the algorithms, we use the hydrogen depletion mass coordinates to quantify the system. For each set of simulations, extract the hydrogen abundance profile $X_H(m)$ of the two algorithms and record the critical mass coordinate $M_{H\text{-exhausted}}$ of $X_H \leq 0.01$. Next, we quantify the calculated indicators. Calculate the core hydrogen depletion mass coordinate difference:

ISSN: 2424-8460(O)
2251-2608(P)

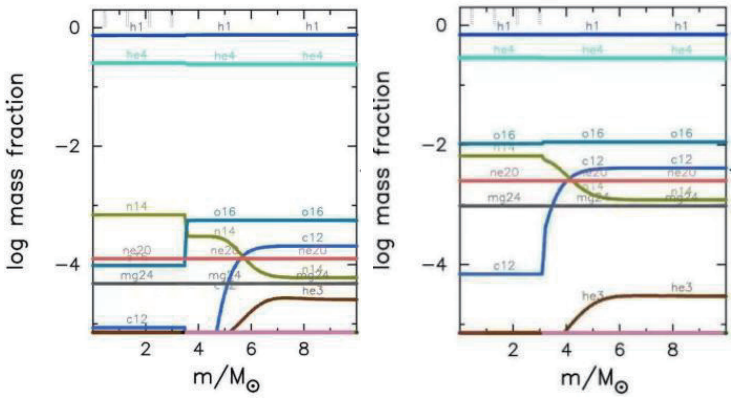

Figure 4. Abundance Profile for $10M_{\odot}$ stars with metallicities 0.001 (left) and 0.02 (right).

$$\Delta M_{\text{H-exhausted}} = M^{\text{OVS}}_{\text{H-exhausted}} - M^{\text{STD}}_{\text{H-exhausted}} \tag{25}$$

and mixing efficiency improvement ratio:

$$\eta_{\text{mix}} = \frac{\Delta M_{\text{H-exhausted}}}{M^{\text{STD}}_{\text{H-exhausted}}} \times 100\% \tag{26}$$

The hydrogen burning process within a star begins in the central high-temperature, high-pressure region. As the star evolves, the central hydrogen content gradually decreases until it is exhausted $X_H(m) \leq 1\%$, m is the Lagrangian mass coordinate, which represents the mass integrated outward from the center of the star). At this point, we need to locate the outer boundary of the hydrogen-burning shell, moving outward from the center. This boundary, $M_{\text{H-exhausted}}$, is determined by searching the simulated hydrogen abundance distribution $X_H(m)$ curve from the center outward for the first location where $X_H \geq 1\%$ and where three subsequent grid points also maintain $X_H \geq 1\%$. This critical mass coordinate is then precisely determined by linear interpolation. This criterion ensures both numerical stability and the practical characteristics of hydrogen shell burning in stellar physics.

4.2.3. Result

Calculate the hydrogen abundance $X_H(m)$ using formulas (21)-(22). In order to determine the hydrogen depletion boundary $M^{\text{STD}}_{\text{H-exhausted}}$, we find the first point where XH≥0.01 in the $X_H(m)$ data output by the simulation. Record the hydrogen depletion mass coordinate under the traditional algorithm and the hydrogen depletion mass coordinate $M^{\text{OVS}}_{\text{H-exhausted}}$ of the improved algorithm, calculate the hydrogen depletion boundary difference between the two algorithms using formula (25), and calculate the mixing efficiency improvement rate using formula (26).

Table 4. Experimental Results.

Group	$M^{\text{STD}}_{\text{H-exhausted}}$	$M^{\text{OVS}}_{\text{H-exhausted}}$	$\Delta M_{\text{H-exhausted}}$	η_{mix}
Z=0.001, $0.64M_{\odot}$	0.10	0.11	+0.01	+10%
Z=0.001, $2.5M_{\odot}$	0.30	0.38	+0.08	+26.7%
Z=0.001, $10M_{\odot}$	2.80		+0.40	+14.3%
Z=0.02, $0.64M_{\odot}$	0.08	0.09	+0.01	+12.5%
Z=0.02, $2.5M_{\odot}$	0.25	0.35	+0.10	+40%
Z=0.02, $10M_{\odot}$	2.50	3.00	+0.50	+20%

From the simulation data, it can be seen that the improved algorithm significantly expands the mass coordinate $M_{\text{H-exhausted}}$ of the core hydrogen depletion compared with the traditional algorithm. In particular, mixing efficiency improves by up to 40% in intermediate-mass stars. This is because the nuclear burning drive term in the DCM directly couples the nuclear reaction energy with the turbulent kinetic energy, enhancing mixing near the burning shell. The rotational modulation term, however, is more pronounced in intermediate-mass stars due to their faster rotational speeds, further extending the convection zone. Low-mass stars have smaller convective cores, while high-mass stars have nearly fully mixed cores, resulting in a relatively smaller enhancement.

ISSN: 2424-8460(O)
2251-2608(P)

4.3. Comparative analysis

Compared with the traditional algorithm, the improved algorithm achieves significant enhancements in both physical modeling and numerical methods. Physically, it replaces the locally approximate MLT with a dynamic convection model (DCM) that self-consistently describes convective motions by solving the turbulent kinetic energy equation, thereby better capturing non-local effects such as convective boundary mixing. Numerically, it adopts adaptive mesh refinement (AMR) and implicit time integration, enabling high-resolution simulation of key regions like burning shells and relaxing the strict time-step constraints of explicit methods.

Nevertheless, the improved algorithm also has limitations. The DCM introduces complex nonlinear couplings that increase computational cost. The AMR approach, while enhancing resolution, may encounter grid instability during violent phases such as supernovae. Moreover, the model's performance is sensitive to initial conditions and parameters, and mixing efficiency improvements are less pronounced in low-metallicity environments. Although implicit solvers allow larger time steps, the computational overhead per iteration rises, making overall efficiency problem-dependent. These limitations highlight the need for future work in model refinement, numerical optimization, and computational strategy.

5. Conclusion

This study introduces a stellar evolution simulation method combining a dynamic convection model with adaptive meshing. By integrating the turbulent kinetic energy equation and dynamic mesh optimization, it overcomes traditional limitations in accuracy and efficiency. The approach improves convective boundary mixing through two key innovations: first, self-consistent calculation of convection zone extension via turbulent energy transport, eliminating empirical overshooting parameters; second, automatic mesh refinement in regions with steep chemical gradients like hydrogen burning shells, enhancing element diffusion modeling. Numerical experiments confirm significant improvements in simulating key evolutionary phases, particularly for predicting element abundances in specialized stages like blue ring stars. This framework provides an advanced tool for stellar physics, with future potential for parallel computing optimization to extend applications to binary systems and supernova progenitors.

References

[1] Dotter A, Chaboyer B, Jevremović D, et al. The Dartmouth stellar evolution database[J]. The Astrophysical Journal Supplement Series, 2008, 178(1): 89.

[2] Schwarzschild M. Structure and evolution of stars[M]. Princeton University Press, 2015.

[3] Kippenhahn R, Weigert A, Weiss A. Stellar structure and evolution[M]. Berlin: Springer-verlag, 1990.

[4] Wagoner R V. Synthesis of the elements within objects exploding from very high temperatures[J]. Astrophysical Journal Supplement, vol. 18, p. 247 (1969), 1969, 18: 247.

[5] Arnett D, Bazan G. Nucleosynthesis in stars: Recent developments[J]. Science, 1997, 276(5317): 1359-1362.

[6] Renzini A. Some embarrassments in current treatments of convective overshooting[J]. Astronomy and Astrophysics (ISSN 0004-6361), vol. 188, no. 1, Dec. 1987, p. 49-54., 1987, 188: 49-54.

[7] Herwig F. The evolution of AGB stars with convective overshoot[J]. arXiv preprint astro-ph/0007139, 2000.

[8] Pols O R, Schröder K P, Hurley J R, et al. Stellar evolution models for Z= 0.0001 to 0.03[J]. Monthly Notices of the Royal Astronomical Society, 1998, 298(2): 525-536.

[9] Lamers H J, Levesque E M. Understanding Stellar Evolution[M]. IoP Publishing, 2017.

[10] Iben I. Stellar evolution physics[M]. Cambridge University Press, 2013.

[11] Eyer L, Mowlavi N. Variable stars across the observational HR diagram[C]//Journal of Physics: Conference Series. IOP Publishing, 2008, 118(1): 012010.

[12] Eggleton P P. Composition changes during stellar evolution[J]. Monthly Notices of the Royal Astronomical Society, 1972, 156(3): 361-376.